

Measuring Electron Energy in Muon-to-Electron Conversion using Holographic Synchrotron Radiation Emission Spectroscopy

Nicholas Cutsail, Johan Vonk, and Vivek Singh*
Department of Physics, University of California, Berkeley - 94720

Yury G Kolomensky
*Department of Physics, University of California, Berkeley - 94720 and
Nuclear Science Division, Lawrence Berkeley National Laboratory, Berkeley - 94720*
(Dated: September 5, 2024)

The coherent conversion of a muon to an electron in a nuclear field has been one of the most powerful methods to search for Charged Lepton Flavor Violation (CLFV). Recent advancements have significantly enhanced the sensitivity of $\mu \rightarrow e$ searches, primarily driven by advancements in muon beamline design and low-mass tracking detectors, which afford exceptional momentum resolution. Nevertheless, the performance of these detectors is inherently limited by electron scattering and energy loss within detector materials. To overcome these inevitable limitations, we propose a novel *holographic* track reconstruction leveraging synchrotron radiation emitted by electrons. Similar to cyclotron radiation emission spectroscopy (CRES) which has demonstrated outstanding energy resolutions for low-energy electrons, our technique relies on a precision measurement of cyclotron frequency, but in a regime where photons are emitted stochastically and are projected onto a 2-dimensional inner surface of a solenoidal magnet. We outline the concept of such a massless holographic tracker and feasibility of employing this innovative detection strategy for $\mu \rightarrow e$ conversion. We also address pertinent limitations and challenges inherent to the method.

I. INTRODUCTION

The Standard Model (SM) of particle physics assumes the fundamental notions of lepton number and flavor conservation [1]. Both are accidental symmetries, and a theoretical framework that explains the underlying symmetry leading to these conservation laws still needs to be discovered. The observation of neutrino oscillations, which is possible only if neutrinos have mass, has confirmed lepton flavor violation in the neutral lepton sector and implies that all processes involving lepton flavor violation should manifest at some level in perturbation theory. Therefore, Charged Lepton Flavor Violation (CLFV) remains a subject of intense theoretical and experimental interest that will offer valuable insights into the nature of the new physics beyond the SM if observed [2–5]. Currently, searches for $\mu^+ \rightarrow e^+\gamma$, $\mu \rightarrow e^+e^-e^+$, and coherent conversion of $\mu^- \rightarrow e^-$ in the field of a nucleus stand out among all CLFV investigations, offering the most stringent constraints [6–8]. These channels have relatively clean final states, consisting only of electrons and photons, and allow an experiment to perform nearly background-free search using high-intensity muon sources. The essence of our study revolves around the experimental identification of $\mu^- \rightarrow e^-$ conversion, highlighting its distinctive experimental advantages alongside inherent complexities. It relies on negative muons from a muon beam captured by a target material, forming muonic atoms that cascade down to the ground state. In the SM, muons decay in atomic orbit (DIO) or undergo

nuclear muon capture. DIO involves the decay of the bound-state muon to an electron and neutrinos, while in nuclear muon capture, the muon combines with a nucleus to produce neutrinos. If $\mu^- \rightarrow e^-$ conversion occurs, an electron is produced without neutrinos. This electron has a specific energy determined by the muon binding energy and the recoil energy of the nucleus:

$$E_{\mu e} = m_{\mu}c^2 - B_{\mu}(Z) - R(A) \quad (1)$$

where $B_{\mu}(Z)$ is the atomic binding energy of the muon and $R(A)$ is the atomic recoil energy for a muonic atom with the atomic number Z and the mass number A . With only a monoenergetic electron in the final state, $\mu^- \rightarrow e^-$ conversion is speculated to provide the ultimate sensitivity to the CLFV process in the long term since, unlike $\mu^+ \rightarrow e^+\gamma$ and $\mu \rightarrow e^+e^-e^+$ processes, it does not suffer from the accidental coincidence background at high muon rates. Additionally, since the muon interacts with quarks in a nucleus, the conversion rate depends on the target nucleus and is model-dependent.

Exceptional experimental progress has been made in the last decade, enabling upcoming experiments like Mu2e [9] and COMET [10] to improve the sensitivity of the $\mu^- \rightarrow e^-$ conversion by four orders of magnitude. This is enabled by the use of a pulsed beam, a novel muon beamline with grated magnetic field, and state-of-the-art low-mass tracking detectors that let the experiments achieve excellent momentum resolution better than 0.2% [11, 12]. The excellent momentum resolution is critical for higher sensitivity since the DIO electrons constitute an intrinsic background that scales with the muon beam intensity. In the endpoint region, the DIO rate varies as $(E_{\mu e} - E)^5$ [13, 14] and can only be suppressed with sufficient momentum resolution for the rel-

* singhv@berkeley.edu

ativistic electron.

Current experiments commonly employ low-mass particle tracking detectors within a magnetic field to precisely track the trajectory of the relativistic electron emitted during conversion, facilitating its momentum measurement. However, the momentum resolution of present-day trackers is inherently limited by fluctuations in the energy loss in the tracking material. Ongoing efforts to further reduce the material budget of these detectors will likely push the current technologies to the limit [15, 16]. Stochastic energy loss widens the conversion signal, necessitating experiments to integrate over a broader region and resulting in increased DIO background; this re-emphasizes the significance of minimizing energy loss and detector resolution.

We present a novel idea of using synchrotron radiation (SR) from the emitted electrons for energy reconstruction, eliminating the need for tracking material and minimizing the effect of energy loss on track reconstruction. Our proposed technique is fundamentally based on a non-destructive measurement of the electron's cyclotron frequency by projecting visible SR photons onto a photosensitive detector located on the inner surface of a solenoidal magnet. Precise measurements of times and positions of a set of stochastic photon hits on a two-dimensional cylindrical surface reconstructs the three-dimensional electron trajectories within the solenoidal volume, a technique akin to holography. The method of non-destructive radiation spectroscopy, in spirit, is similar to the Project 8 experiment [17], which uses Cyclotron Radiation Emission Spectroscopy (CRES) [18] for measuring low-energy electrons from β -decay. However, the implementation of our technique diverges significantly from Project 8, as discussed in the following sections.

II. PROPOSED EXPERIMENTAL APPROACH

Since Mu2e and COMET use Al(Z=13) as a stopping target, we will use $E_{\mu e}$ for muonic Al ($E_{\mu e} \approx 105$ MeV) to elucidate our proposed technique. However, the method can be easily tuned for other nuclei with suitable changes in the experimental parameters, as shown below. The 105-MeV electrons are ultrarelativistic with a high Lorentz factor ($\gamma \approx 205$) and emit SR when subjected to acceleration in a magnetic field. The understanding of SR emitted by a single charged particle is well-established and is used extensively in scientific research. We will summarize the radiation characteristics and refer the readers to comprehensive and excellent textbooks for details [19–21].

We consider hypothetical conversion electrons radially confined within a cylindrical volume permeated by a uniform axial magnetic field (\mathbf{B}). These electrons follow helical trajectories along the magnetic field lines even at ultrarelativistic energies. However, their orbital angular frequencies (ω_L) are reduced due to the relativistic increase in their energy by a factor of γ (Eqn. 2).

$$\omega_L = \frac{eB}{\gamma m_e} = \frac{\omega_G}{\gamma}. \quad (2)$$

In this equation, $\omega_G = eB/m_e$ represents the non-relativistic cyclotron frequency of the electron. The SR emitted by these electrons exhibits a continuous spectrum, with power distributed across a wide spectrum of frequencies. The peak radiation power occurs near the critical frequency (ω_c) [19], defined as:

$$\omega_c = \frac{3}{2}\gamma^3\omega_L = \frac{3eB \sin\theta\gamma^2}{2m_e}. \quad (3)$$

where θ denotes the pitch angle between the electron's velocity and the magnetic field \mathbf{B} . The radiation is spread over a broad spectrum of frequencies around ω_c , with the total power following the distribution:

$$\frac{dP}{d\omega} = \frac{P_s}{\omega_c} \frac{9\sqrt{3}}{8\pi} \frac{\omega}{\omega_c} \int_{\omega/\omega_c}^{\infty} K_{5/3}(z) dz. \quad (4)$$

where $K_{5/3}$ is a modified Bessel function of the second kind of order 5/3. The average rate of photons is given by

$$\dot{N} = \frac{P_s}{\hbar\omega}. \quad (5)$$

Moreover, the angular distribution of the radiation power is highly directional, concentrated within a narrow cone of angle θ_{RMS} in the electron's orbital plane, and emitted predominantly in the direction of its motion.

$$\theta_{\text{RMS}} \sim \frac{1}{\sqrt{2}\gamma} \left(\frac{\omega_c}{\omega}\right)^{0.4}. \quad (6)$$

The SR features outlined above provide the foundation for our proposed experimental approach. The dominant frequency of the synchrotron radiation is enhanced by a factor of $\frac{3}{2}\gamma^3$ compared to cyclotron radiation and results in a significant shift in the radiation spectrum in frequency for muonic conversion electrons; the dominant radiation frequency shifts by $\sim 8 \times 10^6$ for a 105-MeV electron. This shift dramatically alters the detector requirements needed to measure the radiation. For typical magnetic field strengths of 1–3 T, the critical frequency of a 105-MeV electron falls near the optical/UV range (Fig. 1), allowing the use of optical photodetectors for electron radiation measurement.

The highly directional nature of the emitted light allows for direct tracking of the electron's trajectory within a magnetic field in a vacuum environment, making a precise energy reconstruction feasible. This is a drastically different detection scheme from Project 8, where most of the emitted radiation from cyclotron motion is concentrated in a sharp, energy-dependent RF frequency band that can be precisely measured with resonant pickup. However, the power is broadened for SR over a range of

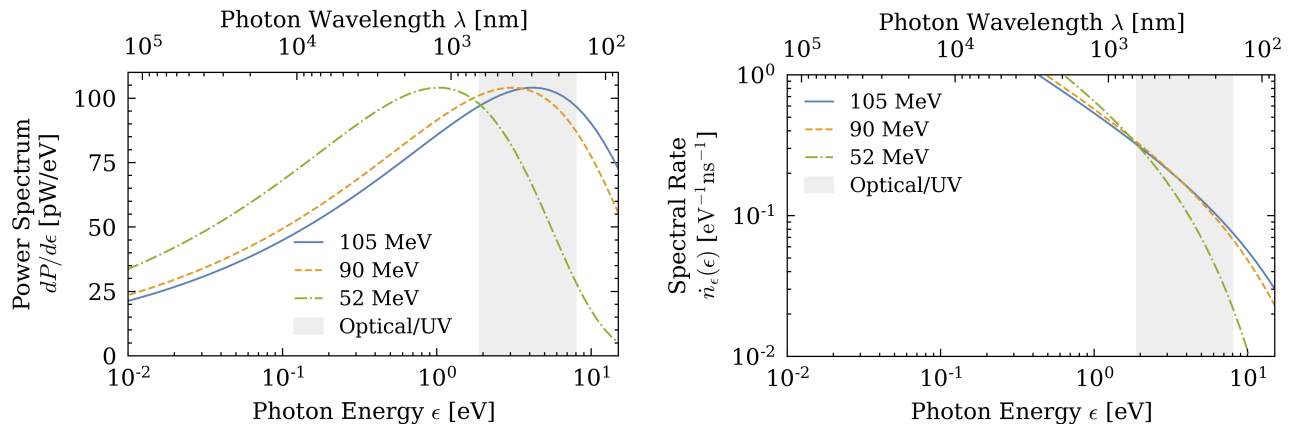


FIG. 1. Spectral distribution of SR emitted from electrons in a 2T magnetic field with a $\theta = \pi/2$ pitch-angle and electron energy E_e of 105 MeV, 90 MeV, and 52 MeV. The 105 MeV electron is approximately equal to the direct conversion endpoint, whereas the 52 MeV electron is characteristic of the Michel decay process. The 105 MeV electron has a spectral power distribution maximized in the optical/UV band of interest. Electrons with lower energies have a correspondingly lower critical frequency, thus contributing less power to the optical/UV band-of-interest.

harmonics of the electron's revolution frequency. Thus, the energies of the SR radiation photons do not precisely encode the energies of the electrons. Instead, we focus on measuring the cyclotron frequency by correlating it to the temporal and spatial distribution of the radiation. Specifically, we propose using optical photodetectors to record individual photon hits rather than the average power distributed over the detector chamber. This is crucial because a 105-MeV conversion electron produces too few optical photons per revolution to yield a meaningful average power distribution (Fig 1). Instead, we must analyze the track as a sparse collection of stochastic photon hits originating from the electron's trajectory. The electron's path is projected onto the detector surface, forming a characteristic "hologram" of its motion (Fig. 2).

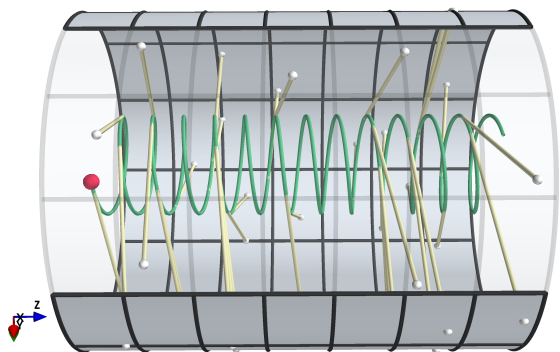


FIG. 2. A simulated conversion electron track is shown inside a hollow photodetector shell. The electron is created at the muon beam stopping target, moving along the magnetic field $\mathbf{B} = B_0 \hat{z}$ in a helical trajectory. Photons are spontaneously emitted by the electron and travel nearly tangentially outwards from the helical path.

While each photon hit does not directly measure the electron's path (as photons are emitted stochastically), the overall pattern of photon hits mirrors that of conventional particle trackers, allowing for similar analysis techniques (Fig. 3).

For 105-MeV electrons in a 2T magnetic field, the cyclotron frequency is $f \approx 0.27$ GHz, corresponding to a period of 3.7 nsec. The energy resolution is determined by the dwell time (length of the detector), the number of detected photons, and the time resolution for each photon hit. Recent advances in optical photon detection technologies make it possible to conceive of a detector with intrinsic energy resolution of better than 10^{-3} (100 keV). For estimates of performance, we use the parameters demonstrated in modern photodetectors such as Large Area Picosecond Photo-Detectors (LAPPDsTM) which offer time resolution of < 50 psec/pixel and pixel sizes of a few mm^2 [22].

III. SIMULATION AND RECONSTRUCTION

In our simulation framework, we define the detector parameters encompassing their geometry, timing, spatial resolution, and quantum efficiency of the photodetector. These parameters define our virtual experimental setup. We then establish the initial conditions for the electrons, assuming an emission point within the target and setting the initial energy for signal electrons at 105 MeV. We model the electrons as being emitted isotropically from the stopping target, but a gradient magnetic field subsequently influences their trajectories. Moreover, we assign random emission times to the electrons. Subsequently, we model the electron paths as helical trajectories within the magnetic field, ignoring radiation damping since the energy loss is negligible. A crucial aspect of our sim-

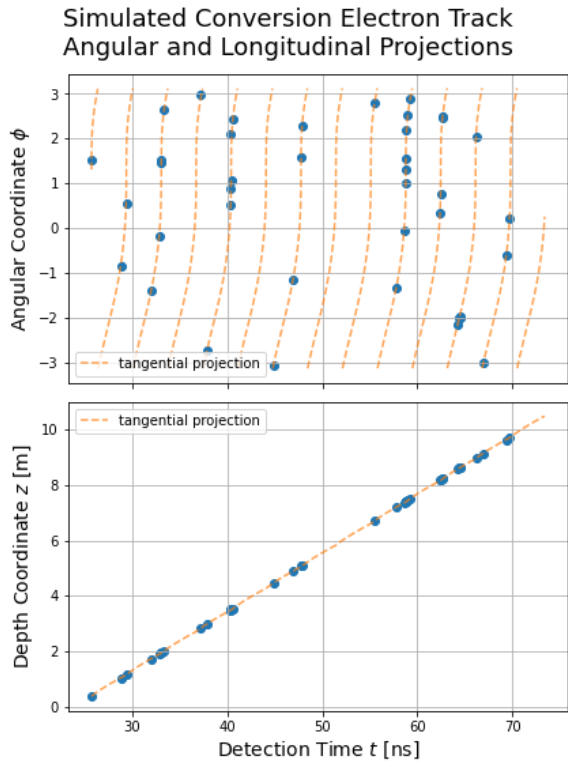


FIG. 3. A simulated conversion electron track is shown. Photons are randomly emitted by the electron, travel in straight paths at the speed of light, and hit the detector at an angular coordinate ϕ , depth-coordinate z , and time t . The photon hits are stochastic and sparse in time and are nearly linear in z vs t .

ulation is calculating the expected number of detected photons. This is achieved by integrating the product of the spectral rate (as depicted in Figure 1) and the photodetector's quantum efficiency over the optical band and then multiplying this result by the electron's dwell time within the detector. To account for the inherent statistical nature of photon detection, we sample a Poisson distribution to simulate the number of detected photons associated with each electron track and we randomize the photon emission times. The next step in our simulation involves determining the directions of the generated photons. We achieve this by sampling the angular and spectral distribution formula for synchrotron radiation as shown below [19].

$$\frac{d\dot{n}}{d\Omega dE} = \frac{\dot{n}}{E} \frac{4\sqrt{3}}{5\pi} \left(\frac{3E}{4E_c}\right)^{\frac{2}{3}} \left[\left(\gamma\psi \text{Ai} \left(\left(\frac{3E}{4E_c}\right)^{\frac{2}{3}} (1+\gamma^2\psi^2) \right) \right)^2 + \left(\text{Ai}' \left(\left(\frac{3E}{4E_c}\right)^{\frac{2}{3}} (1+\gamma^2\psi^2) \right) \right)^2 \right] \quad (7)$$

We then calculate their intersection points with the cylindrical detector with the photon directions established, considering the detector's geometry. We then introduce timing and position errors based on Gaussian distributions that reflect the detector's timing and spatial

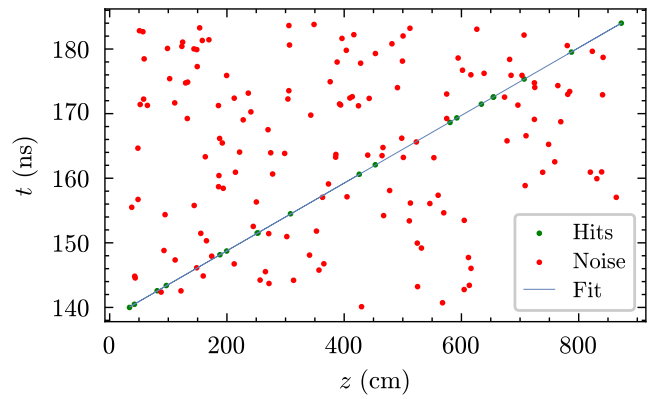


FIG. 4. Example of uncorrelated background rejection with one signal track. An initial time and pitch angle estimate for suitable tracks is obtained using a Hough transform on their z -position vs. time, followed by DBSCAN to identify maxima. This method is robust to background noise and helps separate multiple tracks.

resolution. Additionally, we acknowledge the discretization of position errors due to the pixelation of the detector and justify its negligible impact compared to the broader angular distribution of the photons. The final stage of our simulation involves combining the detected photon hit locations and times from individual electron tracks to create a comprehensive representation of simultaneous tracks.

We initiate the reconstruction process by requiring a minimum number of detected photons. This strategic selection balances the desired reconstruction resolution against the percentage of retained signal tracks (efficiency). Once we identify the suitable tracks, we get an initial estimation of their emission time and pitch angle by performing a Hough transform [23] on the linear relationship between the z -position and time (t) for each track, followed by the application of DBSCAN (Density-Based Spatial Clustering of Applications with Noise) [24] to identify maxima in the resulting Hough space. This approach offers the advantages of being relatively resistant to random background photons and facilitating the separation of multiple tracks (Fig. 4).

The initial time is extracted from the x -intercept of the fitted line, while the pitch angle is derived from its slope using the relation

$$\theta = \arccos \left(\frac{dz}{dt} \cdot \frac{1}{\beta c} \right) \approx \arccos \left(\frac{\widehat{dz}}{dt} \cdot \frac{1}{c} \right). \quad (8)$$

We also quantify the success rate of this initial estimation and elaborate on how the presence of background photons influences it. With initial estimates for the initial time and pitch angle, we employ a maximum likelihood fit to refine our reconstruction further.

We perform "toy" simulations to elucidate relations between energy resolution and experimental conditions. First, the primary electrons are generated according to

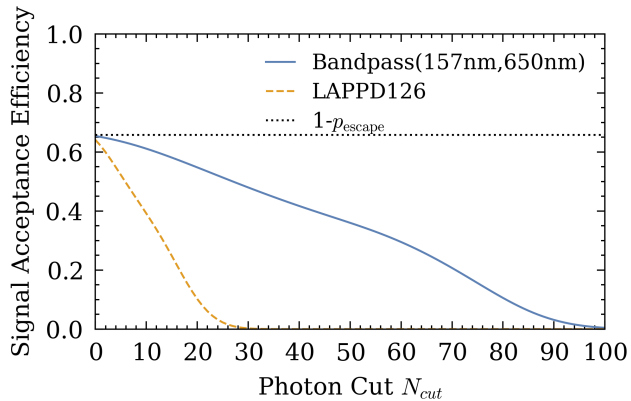


FIG. 5. Probability of accepting a 105 MeV conversion electron under a photon cut $n_{\text{hits}} > N_{\text{cut}}$. The acceptance probabilities are upper-bounded (p_{escape}) due to the fraction of backward-moving electrons that fail to turn around in the graded field.

the specified momentum distributions (either a delta function for $\mu \rightarrow e$ conversion electrons, or Michel and DIO spectra). The constant magnetic field and small radiative losses ($\ll 1\%$) allow us to treat electron motion as a simple helix. Photons are emitted randomly according to the synchrotron distributions and are detected by a cylindrical photodetector shell.

We use a simple model for the sensitive detector based on state-of-the-art technology. Large Area Picosecond Photo-Detectors (LAPPDsTM) are capable of capturing photon hits with the high spatial and temporal resolutions necessary to furnish a useful hologram. In particular, LAPPDs boast position resolutions ~ 3 mm, timing resolutions ~ 50 ps, dark count rates $\lesssim 1$ kHz/cm², and quantum efficiencies up to 25% [22]. We model these responses as Gaussian.

For each simulated track, we reconstruct energies using the maximum likelihood method. The detection likelihood for each hit $\mathcal{L}(\theta, \lambda)$ is modeled with dependence on critical track parameters θ and photon nuisance parameters λ . Then, the fit energy is taken to be that which maximizes the likelihood $\theta^* = \text{argmax}_{\theta} \mathcal{L}(\theta)$.

Since the likelihood function may contain several local minima, we use a multi-step seeding process. First, we take a Hough transform to fit the linear z vs t response (see Fig. 2). The fit x -intercept corresponds to the initial time when the electron is emitted, while the slope is related to the pitch angle (θ) by $\theta = \arccos(\frac{\text{slope}}{c})$. Next, using a precomputed grid of template tracks in energy and pitch angle, we minimize the negative log likelihood interpolating between the nearest tracks. It is also important to note that the likelihood is affected both by detector resolutions and the geometric angular spread inherent in the synchrotron emissions.

To proceed with our analysis, we set the detector parameters to experimentally practical values: $B = 2\text{T}$,

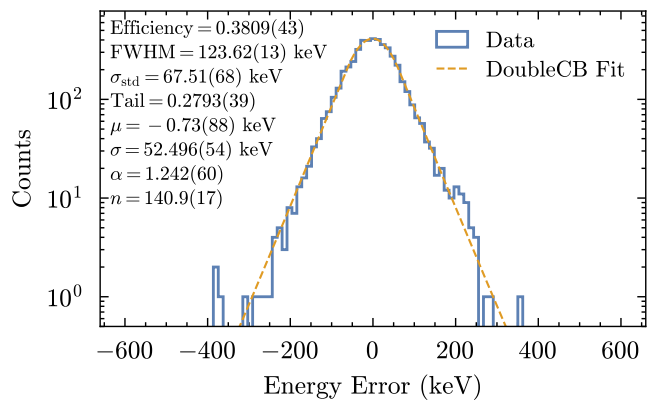


FIG. 6. In a numerical experiment where detector parameters were held constant, we simulated 13,000 tracks. Out of these, 8,719 were successfully reconstructed. Applying stricter criteria—requiring at least 14 detected photons, a grid uncertainty below 400 keV, and a Munit uncertainty below 350 keV—left us with 4,952 tracks that passed all filters (see text for details).

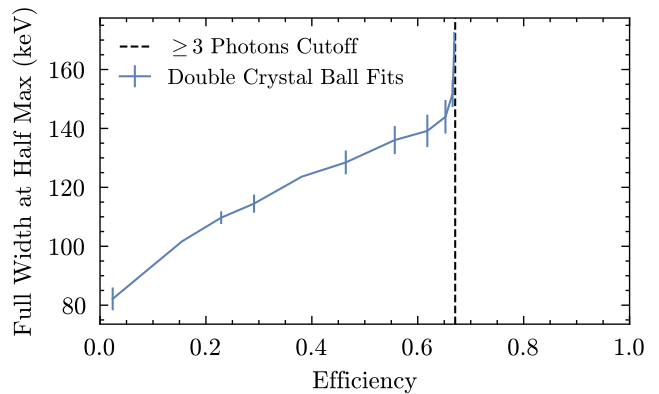


FIG. 7. The resolution of the fit, measured by the full width at half maximum (FWHM), improves as the minimum number of required photon hits increases. However, this comes at the cost of reduced efficiency. Due to the nonlinear relationship between ϕ and t , a minimum of 3 photon hits is necessary for fitting, and the FWHM increases dramatically as we approach this minimum. This figure was generated in the absence of background hits.

the length of the detector solenoid $L = 10\text{m}$, the gradient magnetic field with the target region at $B = 2.25\text{T}$, and LAPPD photosensors. Under these conditions, track photon counts vary drastically due to Poisson statistics and a strong dependence of dwell time on pitch angle. Low-count tracks reconstruct poorly, whereas high-count tracks reconstruct with better resolution, so the hit count constitutes an essential track quality measure. With the goal of surpassing Mu2e's $\mathcal{O}(100 \text{ keV}/c)$ momentum resolution, we require ≥ 10 hits to constrict the resolution while maintaining adequate acceptance efficiency (Fig. 5). Since the average photon count has a strong monotonic dependence on pitch angle, the photon count

cut roughly corresponds to a minimum pitch-angle cut around 54° .

The use of a graded field maps some of the backward-moving decay electrons into this pitch-angle acceptance region, increasing the overall acceptance efficiency. With electron momenta fully randomized and photon count determined by the associated SR rate and Poisson distribution, we reconstruct simulated 105 MeV conversion electrons with a resolution of $\sigma = 52.4 \text{ keV} \pm 0.5 \text{ keV}$ (FWHM $\approx 123 \text{ keV}$) at 67% post-cut efficiency, giving a total $\pm 3\sigma$ reconstruction efficiency of approximately 38% (Fig. 6). Higher resolution (lower FWHM) is achievable by requiring more photon hits, though this leads to decreased efficiency as fewer events meet the stricter threshold (Fig. 7).

IV. BACKGROUNDS

A very appealing feature of SR-based detection is that it is insensitive to any particle background other than electrons. The primary background sources are DIO electrons, which can be separated based on their lower energies, and random hits due to the photodetector's dark rates. LAPPDs based on microchannel plates are relatively insensitive to direct hits by neutrons, protons, and X-rays. In the first step of reconstruction, we use a Hough transform to fit the initial slope and time. Introducing background, we can use a clustering method such as DBSCAN to find all tracks in the data. This method shows promising robustness against background hits and good potential for accurate track separation, achieving success rates exceeding 50% in our initial testing. Further yield improvements may be possible by implementing a likelihood-based approach.

The dark rate hits are uncorrelated and do not form tracks; their effect on energy resolution is negligible.

V. CONCLUSION AND FUTURE OUTLOOK

A typical energy resolution for the holographic synchrotron radiation detector is shown in Fig. 6. With the cut on the number of photons of $N_\gamma > 14$, we project an energy resolution (Gaussian σ) of 52 keV and the selection efficiency of 38%. This performance exceeds that of the current Mu2e detector and is adequate for the next-generation experiment Mu2e-II [25].

We note that the HSRES technique offers a number of advantages. First, since it is relatively insensitive to the non-relativistic particles, it can tolerate the beam-related backgrounds generated during the beam "flash". Therefore, this technique could open a window to explore heavy stopping targets such as Au, which correspond to short muon capture lifetimes. In addition, placing the HSRES detector in a relatively high magnetic field of 2 T may allow a conventional tracker-calorimeter detector similar to Mu2e to be located downstream in a lower magnetic field region. Thus, the HSRES technique is compatible with conventional tracking detectors. The use of both would allow additional background rejection capabilities, improve the combined energy resolution, and allow a robust identification of the signal in case of discovery.

VI. ACKNOWLEDGEMENTS

The authors would like to thank the Project 8 collaboration for the inspiration, Elise Novitski for technical discussions regarding the CRES technique, and Marjorie Shapiro for asking whether the technique could be applied to Mu2e and stimulating this development. We are indebted to the Mu2e collaboration for making the concept of late Vladimir Lobashev a reality and motivating us to pursue it further. This work was supported by the US Department of Energy (DOE) Office of High Energy Physics under Contract No. DE-SC0018988, and by the Physics Department at the University of California, Berkeley. This research used the resources of the National Energy Research Scientific Computing Center (NERSC).

-
- [1] S. Navas, C. Amsler, T. Gutsche, C. Hanhart, J. Hernández-Rey, C. Lourenço, A. Masoni, M. Mikhasenko, R. Mitchell, C. Patrignani, *et al.*, *Physical Review D* **110**, 030001 (2024).
 - [2] A. de Gouvea and P. Vogel, *Prog. Part. Nucl. Phys.* **71**, 75 (2013), arXiv:1303.4097 [hep-ph].
 - [3] W. J. Marciano, T. Mori, and J. M. Roney, *Ann. Rev. Nucl. Part. Sci.* **58**, 315 (2008).
 - [4] R. H. Bernstein and P. S. Cooper, *Phys. Rept.* **532**, 27 (2013), arXiv:1307.5787 [hep-ex].
 - [5] L. Calibbi and G. Signorelli, *Riv. Nuovo Cim.* **41**, 71 (2018), arXiv:1709.00294 [hep-ph].
 - [6] A. M. Baldini *et al.* (MEG), *Eur. Phys. J. C* **76**, 434 (2016), arXiv:1605.05081 [hep-ex].
 - [7] U. Bellgardt *et al.* (SINDRUM), *Nucl. Phys. B* **299**, 1 (1988).
 - [8] W. H. Bertl *et al.* (SINDRUM II), *Eur. Phys. J. C* **47**, 337 (2006).
 - [9] L. Bartoszek *et al.* (Mu2e) 10.2172/1172555 (2014), arXiv:1501.05241 [physics.ins-det].
 - [10] R. Abramishvili *et al.* (COMET), *PTEP* **2020**, 033C01 (2020), arXiv:1812.09018 [physics.ins-det].
 - [11] M. Yucel (Mu2e), *PoS PANIC2021*, 430 (2022).
 - [12] A. Volkov, P. Evtoukhovich, M. Kravchenko, Y. Kuno, S. Mihara, H. Nishiguchi, A. Pavlov, and Z. Tsamalaidze,

- Nucl. Instrum. Meth. A **1004**, 165242 (2021).
- [13] O. U. Shanker, *Phys. Rev. D* **25**, 1847 (1982).
- [14] A. Czarnecki, X. Garcia i Tormo, and W. J. Marciano, *Phys. Rev. D* **84**, 013006 (2011), [arXiv:1106.4756 \[hep-ph\]](#).
- [15] N. Tsverava, G. Adamov, D. Chokheli, H. Nishiguchi, T. Toriashvili, and Z. Tsamalaidze, (2024), [arXiv:2403.18097 \[physics.ins-det\]](#).
- [16] D. Ambrose, G. Tassielli, M. Kargiantoulakis, M. Yucel, K. Heller, S. Giovannella, F. Happacher, S. Miscetti, D. N. Brown, and J. Popp, *Letter of Interest for Snowmass 2021* (2020).
- [17] A. Ashtari Esfahani *et al.* (Project 8), *J. Phys. G* **44**, 054004 (2017), [arXiv:1703.02037 \[physics.ins-det\]](#).
- [18] B. Monreal and J. A. Formaggio, *Phys. Rev. D* **80**, 051301 (2009), [arXiv:0904.2860 \[nucl-ex\]](#).
- [19] A. Hofmann, *The Physics of Synchrotron Radiation*, Cambridge Monographs on Particle Physics, Nuclear Physics and Cosmology (Cambridge University Press, 2004).
- [20] H. Wiedemann, Synchrotron radiation, in *Particle Accelerator Physics: I Basic Principles and Linear Beam Dynamics II Nonlinear and Higher-Order Beam Dynamics* (Springer Berlin Heidelberg, Berlin, Heidelberg, 2003) pp. 647–686.
- [21] A. A. Sokolov, I. M. Ternov, and C. W. Kilmister, *Radiation from relativistic electrons* (American Institute of Physics, 1986).
- [22] A. V. Lyashenko *et al.*, *Nucl. Instrum. Meth. A* **958**, 162834 (2020), [arXiv:1909.10399 \[physics.ins-det\]](#).
- [23] P. V. C. Hough, *Conf. Proc. C* **590914**, 554 (1959).
- [24] M. Ester, H.-P. Kriegel, J. Sander, X. Xu, *et al.*, in *kdd*, Vol. 96 (1996) pp. 226–231.
- [25] K. Byrum *et al.* (Mu2e-II), in *Snowmass 2021* (2022) [arXiv:2203.07569 \[hep-ex\]](#).